Interfacial oxidation and boundary amorphization deposition mechanisms of GaN powder on metallic substrate by low-pressure cold spraying

Shaoyun Zhou, Jiayu Sun, Chrystelle Bernard, Hao Lin, Hiroki Saito, Takamichi Miyazaki, Yuji Ichikawa, Kazuhiro Ogawa

Interfacial oxidation and boundary amorphization deposition mechanisms of GaN powder on metallic substrate by low-pressure cold spraying

Shaoyun Zhou[a], *Jiayu Sun*[b,c], *Chrystelle Bernard*[a,d,e,*], *Hao Lin*[a], *Hiroki Saito*[a], Takamichi Miyazaki[f], Yuji Ichikawa[a], Kazuhiro Ogawa[a,d]

[a]*Fracture and Reliability Research Institute, Tohoku University, Sendai, Japan*

[b]*Department of Materials Processing, Graduate School of Engineering, Tohoku University, Sendai, Japan*

[c]*Institute for Materials Research, Tohoku University, Sendai, Japan*

[d]*ELyTMaX UMI 3757, CNRS – Université de Lyon – Tohoku University, International Joint Unit, Tohoku University, Sendai, Japan*

[e]*Frontier Research Institute for Interdisciplinary Sciences, Tohoku University, Sendai, Japan*

[f]*Technical Division Instrumental Analysis Group, School of Engineering, Tohoku University, Japan*

*Corresponding author: Chrystelle Bernard

E-mail address: chrystelle.bernard@rift.mech.tohoku.ac.jp (C. Bernard).

Current address: Fracture and Reliability Research Institute, Tohoku University, 6-6-11-703, Aoba, Aramaki, Aoba-ku, Sendai 980-8579, Japan

Abstract

Understanding powder adhesion mechanism in cold spray is primordial to control the coating formation. Previous studies have suggested that metallic coatings are governed by metallurgical bonding, but no consensus has been established regarding the bonding mechanisms of ceramic particles. In this study, the deposition mechanism of agglomerated gallium nitride (GaN) particles cold sprayed on stainless steel substrates was investigated. The evolution of the oxide layer thickness and coating/particle microstructures were analyzed by X-ray photoelectron spectroscopy and transmission electron microscopy. The results revealed that although mechanical interlocking and coating thickness were enhanced by the substrate surface roughness, grain refinement was not the key factor for the brittle particle deposition, considering the diameter of the nano-sized particles. Instead, a new interfacial oxide layer was formed because of the destruction and removal of native oxide films upon impact. Local heteroepitaxy, which occurred near the interface of the newly formed gallium oxide, enhanced the coating formation. Compared with the GaN feedstock, the coating exhibited boundary amorphization and a high dislocation density induced by the high strain rate. Thus, this study proposed considerable insight into the formation mechanisms of cold-sprayed GaN coatings, which can support a more expanded range of ceramic/metal combinations in the future.

Keywords:

Cold spray

Gallium nitride (GaN)

Deposition mechanisms

Ceramic particles

Oxidation

1. Introduction

As an innovative additive manufacturing method, the cold spray technique is highly dependent on the high-velocity impact of particles for bonding to substrates [1]. Considerable progress has been achieved in processing control, practical applications, and fundamental mechanisms of cold spray since its discovery in the 1980s [1–3]. Compared with other additive manufacturing methods, such as the thermal spray technique, direct energy deposition, selective laser melting, and electron beam melting, cold spray exhibits several technological advantages [4]. Specifically, its self-consolidation capacity of solid materials does not involve the melting of the particles which concurrently build up through layer-by-layer coating fabrication in the solid state [5,6]. Therefore, the defects that lead to a detrimental influence, such as oxidation, phase transformation, and thermal residual stress, are effectively reduced in the final cold-sprayed coatings [1,7].

The elucidation of the deposition mechanism has always been one of the main focuses for technological breakthroughs in cold spray applications [1]. Compared to other interfaces, the metal/metal interface has been extensively studied [8]. The metal/metal interface induced by the cold-spray process is governed by nanoscale metallurgical reactions arising from localized high-strain-rate plastic deformation. Consequently, the natural oxide films are destroyed to induce metallic bonding through creating direct metal-on-metal interfacial contact [1,8–12].

Conversely, scarce studies have focused on the high-velocity impact of brittle ceramic particles owing to the difficulties of deforming them plastically. Nowadays, combining ceramics with dissimilar materials is important for various technological products in the energy, bio-medical, and transport sectors [4-6,9,13] to increase structure performance and improve functionalities. Meanwhile, some uncontrolled thermal decomposition at elevated temperatures could be avoided during the cold spray process, thereby decreasing energy consumption. Therefore, the cold spray process appeals to be promising and novel for the combinations of ceramics with other materials. Moreover, understanding the deposition mechanisms of ceramic particles on metallic substrates is crucial to expand the application range of such coatings. If severe plastic deformation and destruction of the oxide film are requirements for the metal bonding, then the formation of the ceramic coating through cold spraying involves other mechanisms [13]. Currently, it is widely assumed that the critical requirements for forming ceramic coatings by the cold-spray process are a vacuum chamber or the use of agglomerated powder [14–17]. As for the vacuum cold spray technique, Park et al. [18] identified that the deposition mechanisms are mainly governed by plasticization and fragmentation at high strain rates and high pressures induced by hypervelocity impact. Akedo [19] explained that the surface chemistry and surface activation by the formation of a new surface through particle impact dominate the mechanism of particle binding. Winnicki et al. [20] reported that powder agglomeration, rather than fine primary particles, is the decisive factor in the cold spray process under atmospheric pressure conditions. Under impact, the deformation mechanisms of ceramic materials composed of nanoparticles involve particles sliding over particles, leading to densification of the coating. Besides, the coating formation (first layer) relies on substrate deformation and mechanical interlocking [21]. Yamada et al.

[22] also proposed significant principles for the adhesion of ceramic particles by cold spray. They demonstrated that aggregated particles and porous structures are critical to facilitating particle flattening for coating formation.

In our previous works, we successfully fabricated nanoporous GaN coatings via the low-pressure cold spray technique on various substrates [23,24]. Among them, stainless steel 304 was selected because of the easier particle deposition and higher particle deposition efficiency for GaN coatings formation [23,24]. The deposition behavior of a single isolated particle has been studied through the formation of splat tests. The deposition of the GaN particles was possible under relatively high gas pressure and temperature. The particle deposition appears to depend on the disintegration of super-agglomerated particles upon impact. In addition, the high impact velocity of the particle did not involve any phase transformation in the coating. Therefore, the photocatalytic properties of the powder remained in the coating and were even enhanced compared to the powder. This is due to a higher surface-to-volume ratio of the coating controlled by the coating's roughness and thickness. However, the deposition mechanisms at the nanoscale of the GaN powder on the metallic substrate were not well established, especially in the possible detrimental effect of an oxide layer and the chemical states of specific positions during the coating build-up. Thus, a thorough analysis of the deposition mechanisms using higher spatial resolution experiments is imperative [9].

In this study, GaN particles were cold sprayed onto stainless steel 304 substrates to explore the bonding mechanism. X-ray photoelectron spectroscopy (XPS) and transmission electron microscopy (TEM) were performed to investigate the interfacial microstructure and oxide layer thickness evolution from the GaN feedstock, substrate, to coatings at the nanoscale. The bonding mechanisms of the (i) cold-sprayed nitride

agglomerated ceramic powder onto metallic substrates and (ii) coating build-up were briefly proposed.

2. Materials and methods

2.1 Powders and substrates

GaN powder (Toshima Manufacturing Co., Ltd., Saitama, Japan) was used as the feedstock to develop GaN coatings using the low-pressure cold spray (LPCS) technique. The morphology of the GaN feedstock powder was characterized through field-emission scanning electron microscopy (FE-SEM, Hitachi SU-70, Tokyo, Japan), operated at 10 kV accelerated voltage. At high magnification (see Fig. 1a), the nano-sized particles were shaped with an average cross-sectional area of 0.045 μm^2 (measured by open-source software ImageJ). They were naturally agglomerated into ellipsoidal micro-sized particles (see Fig. 1b) with a mean particle length of 1.97 ± 0.013 µm and a mean particle width of 0.74 ± 0.086 µm (the ratio of the semi-major length to the semi-minor length was equivalent to 2.66) [23,25]. Nano-porous super-agglomerated particles (Fig. 1c), also observed in the particle feedstock, were formed thanks to the agglomeration of micro-sized particles due to the combined action of Van der Waals forces and electrostatic surface charge [23,26]. The particle size distribution of the feedstock, obtained by granulometry test by Nikkiso Co. Ltd. (Tokyo, Japan), is provided in Fig. 1d [23].

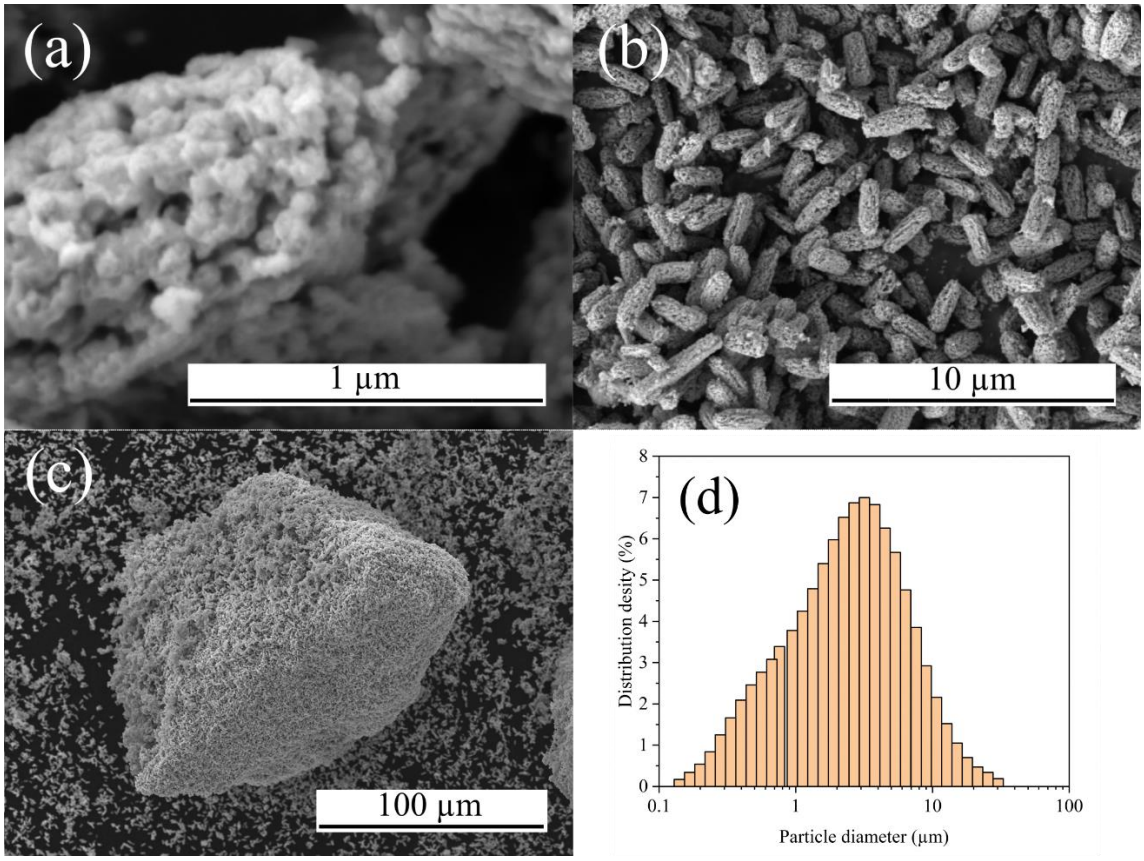

Fig. 1. Scanning electron microscopy (SEM) images of the GaN feedstock. (a) nano-sized particles (average cross-sectional area: 0.045 μm^2), (b) agglomerated micro-sized particles (average particle length: 1.97 ± 0.013 μm), (c) super agglomerated particle, and (d) particle size distribution of the GaN feedstock.

Stainless steel 304 was chosen as the substrate as it proved to be the most suitable for the deposition of GaN powder compared to aluminum or Indium tin oxide (ITO) glass [23,24]. Prior to the coating deposition process, the as-received stainless steel 304 substrates were sandblasted using alumina powder to roughen the surface and promote adhesion. The substrate surface roughness was measured using a surface profilometer (Surfcorder SE300, Kosaka Laboratory Ltd., Tokyo, Japan), and the results are summarized in Table 1. The Vickers hardness of the sandblasted stainless steel substrates

was measured at 216 HV using a microhardness testing system (Fischerscope HM2000, Helmut Fischer) [27]. Before cold spray experiments, the substrates were degreased for 10 min in acetone using ultrasound to eliminate any sources of contamination.

Table 1

Substrates surface roughness before low-pressure cold spray process.

Parameter		As-received substrate	Sandblasted substrate
Substrate roughness	Ra (µm)	0.12 ± 0.01	1.99 ± 0.28
	Rz (µm)	1.31 ± 0.23	19.81 ± 3.87

2.2 Cold spray conditions

The DYMET-423 apparatus (Obninsk Center for Powder Spraying, Obninsk, Kaluga, Russia) was used for LPCS experiments. The system contains an internal gas heater in the spraying gun, a customized converging-diverging nozzle, and a powder feeder. Compressed air was used as the carrier gas during the process.

According to our previous study [23], the best spray conditions to obtain GaN coating by low-pressure cold spray are 400°C and 0.6 MPa for the gas temperature and pressure, respectively. Therefore, the same spray conditions were used in this study to fabricate the coatings. Spraying parameters, including chamber gas pressure and temperature, powder feeding rate, traverse speed, stand-off distance, and pass number, are listed in Table 2. After spray, the specimens were hot mounted with poly fast resin, grounded, and subsequently polished with colloidal silica suspension to characterize the coating microstructure by FE-SEM (Hitachi SU-70, Tokyo, Japan).

Table 2

Cold spray parameters for low-pressure cold spray tests.

Parameter	Values
Gas type	Compressed air
Powder feeding rate (g/s)	0.019
Gas pressure (MPa)	0.6
Gas temperature (°C)	400
Traverse speed, TS (mm/s)	20
Stand-off distance, SoD (mm)	20
Pass number	16

2.3. Feedstock and coating microstructural characterization

The X-ray photoelectron spectroscopy (XPS, Physical Electronics QUANTUM 2000) analysis provides elemental identification and valuable quantitative and chemical information on the specimen surface. By integrating the XPS measurements with ion sputtering, obtained depth distribution information can analyze the oxide film evolution from feedstock and substrate during the cold spray process. A monochromatic Al Kα source with an initial photon energy of 1486.6 eV and a 2 kV argon ion beam was used to excite the photoelectron emission and collect the depth profile (without neutralization). The sputtered area was approximately 2×2 mm^2. The data collection area was approximately 100 μm in diameter with a sputtering rate of 3.23 nm min^{-1} vs. SiO_2 [28]. All XPS spectra were analyzed using MultiPak software (ULVAC-PHI Co. Ltd.). After subtracting the Shirley-type background, the core-level peaks were further calibrated against C1s (284.8 eV). Each XPS spectrum was fitted with a combination of Gaussian and Lorentzian distribution functions [29] to account for the non-symmetry of the peak.

The thickness of the natural oxide layer on the surface of the GaN feedstock, stainless steel substrate, and cold-sprayed coatings was measured depending on the full width at half-maximum (FWHM) [28,30,31].

The feedstock and coating surface up to 1 μm depth were investigated using XPS. However, it is difficult to obtain information regarding the feedstock, inner coating structure, and coating/substrate interface. Therefore, thin lamellae were prepared by lifting from the GaN feedstock and cold-sprayed GaN coatings using focused ion beam (FIB) milling. Subsequently, TEM was performed to identify and quantify the oxide layer presence and thickness of the nano-sized particle/particle interface for the feedstock sample and the particle/particle and particle/substrate interfaces for the coating sample.

Transmission electron microscopy (TEM, JEOL JEM-2100F) observation was carried out using a 200 kV field-emission gun microscope [32]. A scanning transmission electron microscopy (STEM) system, a high-angle annular dark-field (HAADF) detector, and a high-resolution transmission electron microscopy (HRTEM) CCD camera (Gatan; MODEL830 ORIUS SC200) were used [32]. The atomic concentration of each element was determined after integrating the peak area obtained by the HAADF-STEM energy-dispersive X-ray spectroscopy (HAADF-STEM-EDS) line scanning. The corresponding STEM-EDX mapping image for each element intensity was obtained with a spot size of 1 nm and 15 seconds per step dwell time. A fast Fourier transform (FFT) was conducted to identify the crystal or amorphous structures in tiny areas using the software Gatan DigitalMicrograph [30], and therefore, obtain more information regarding the microstructure of the feedstock and coating interfaces.

3. Results

3.1 Cross-sectional morphology of coatings

The SEM images of the GaN coating cross-sections of the as-received and sandblasted substrates are illustrated in Fig. 2. At a spray pressure and temperature of 0.6 MPa and 400°C, respectively (see Table 3), the coating thickness reached 10.4 ± 2.8 µm on the as-received substrate and 13.3 ± 3.0 µm on the sandblasted substrate, respectively.

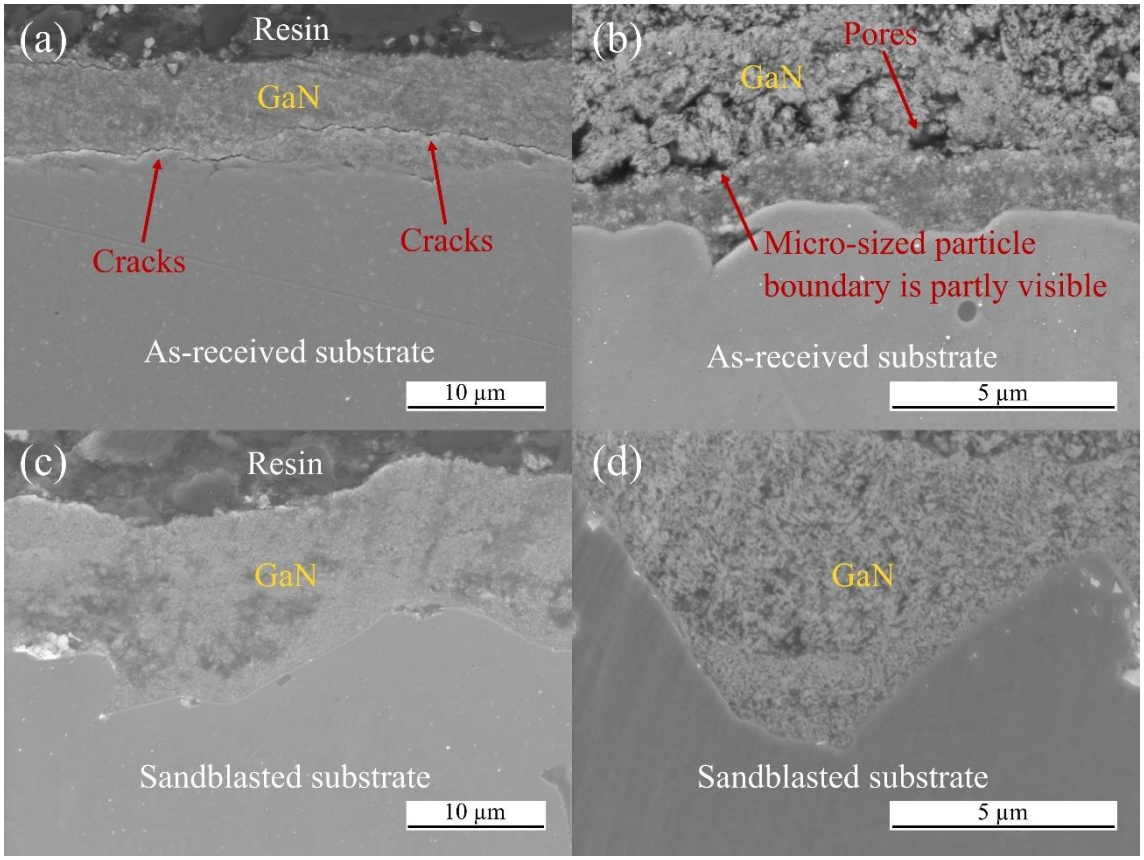

Fig. 2. Cross-sectional SEM images of the GaN coating deposited by low-pressure cold spray on (a-b) as-received and (c-d) sandblasted stainless steel substrates. On the as-received substrate, the coating exhibits micro-cracks and porosity close to the substrate/coating interface. Micro-sized particles are visible. On the contrary, on the sandblasted substrates, the coating appears dense without neither cracks nor micro-sized porosity.

Table 3

Coating roughness and thickness after the low-pressure cold spray process.

Parameter		As-received substrate	Sandblasted substrate
Coating roughness	Ra (μm)	1.73 ± 0.22	2.01 ± 0.23
	Rz (μm)	12.46 ± 1.19	16.74 ± 3.28
Thickness (μm)		10.4 ± 2.8	13.3 ± 3.0

As illustrated in Fig. 2a, visible cracks within the coating on the as-received substrate are observed. Notably, the thickness of the GaN coatings on the sandblasted substrate (Fig. 2c) was enhanced compared to the as-received substrate (Fig. 2a). It is attributed to the roughness increased by sandblasting, thereby strengthening the particles interlocking near the unevenness of the surface [23,33,34]. Moreover, rather than some pores observed between micro-sized particles in Fig. 2b, the boundaries of the micro-sized particles in Fig. 2d became more ambiguous owing to the severe solid consolidation of the tamping effect induced by the continuous impact of particles [14,35,36]. Above all, the mechanical interlocking and thickness of the coatings are mainly governed by the primordial substrate surface roughness [23].

These observations revealed that the coating formation is primarily through severe fragmentation and coordinated deformation of the micro-sized agglomerated and super-agglomerated particles. The continuous impact of the subsequent particles induced strong particle/particle bonding [14,37,38]. Mechanical interlocking appeared to be effectively developed under the sandblasted substrate surface during the cold spray process. Moreover, given the intrinsic porosity of the feedstock and the fact that the remaining

kinetic energy after partial consumption is not sufficient for coordinated deformation, nanoscale voids still appeared within the coatings [14].

3.2 Characterization of the GaN particle size from feedstock to coating

Previous studies suggested that grain refinement induced by fragmentation is essential for the deposition of brittle particles during the spray process [9,14,39,40]. To revisit the viability perspective of the grain refinement for GaN coating deposition, TEM is carried out to reassess the evolution of the particle size from feedstock to coatings.

Fresnel contrast analysis is an effective method for identifying the particle boundary, nano-sized cavities, and evaluating the grain diameter [41,42]. Over-focused (Δ f = 15000 nm), focused (Δ f = 0), and under-focused (Δ f = -15000 nm) TEM images for the GaN feedstock and coatings are illustrated in Fig. 3.

According to our previous study [23], the crystallite size of the GaN feedstock and cold-sprayed coatings, evaluated by X-ray diffraction (XRD), is in the same order of magnitude (see Table 4). Besides, the evaluation of the particle's microstructure by TEM image analysis using ImageJ software estimates the average GaN grain diameter (nano-sized particles) at 70 nm in the GaN feedstock and coatings (see Table 4). Thus, no significant fragmentation appears for the nano-sized particles during the low-pressure cold spray. This could be attributed to the size effect of the ductile-brittle transition for nano-ceramic particles. The fracture strength gradually increases with the decrease of particle size [43,44,45]. Consequently, during the cold spray, the kinetic energy is mainly absorbed through severe fragmentation and coordinated deformation of loosely agglomerated GaN powder (micro-sized and super-agglomerated particles).

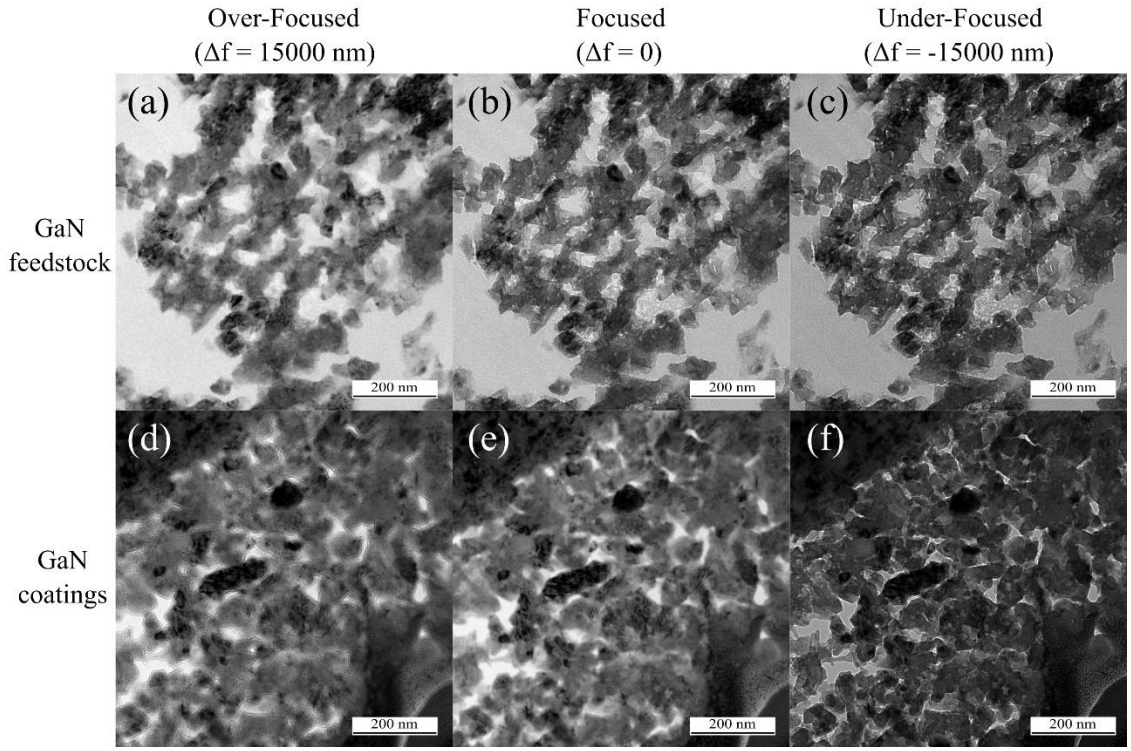

Fig. 3. Fresnel contrast of the (a–c) GaN feedstock and (d–f) GaN coatings at the subtraction of over-focused, focused, and under-focused images, respectively.

Table 4

Average crystallite size and average grain diameter of the GaN feedstock and cold-sprayed coatings evaluated by XRD [23] and TEM analysis.

Specimen	Crystallite size (nm) (XRD, [23])	Grain diameter (nm) (TEM, this study)
GaN feedstock	19.9	75.9 ± 15.5
GaN coatings	18.3	69.2 ± 17.6

3.3 Oxide layer thickness evolution from feedstock to coating

The oxide layer thickness of the feedstock particles, substrate, and coating was measured through XPS and TEM. In XPS, a large-area aperture was used. Thus, the outer oxide layer thickness was interpreted as an average over the feedstock sample encompassing a large number of particles. In comparison, TEM measurements were performed at a specific position approximately 10 μm in diameter, from which thin lamellas were lifted out. Therefore, the oxide layer thickness within the agglomerated particles of feedstock or near/far from the interface of the coating was assessed [12].

The depth-wise element distribution obtained by XPS for the stainless steel 304 substrate surface, GaN feedstock surface, and cold-sprayed coating surface are displayed in Fig. 4. While sputtering from the outermost surface by XPS, the oxygen concentration gradually decreased and stabilized in the inner layer (Fig. 4). The oxide film thickness was determined by the FWHM of the oxygen concentration and the corresponding sputtering time [28,30,31]. Therefore, the original oxide layer thickness of the stainless steel substrate was approximately 12.10 nm. The outer layer was initially enriched in oxygen with slight concentrations of Fe and Cr. Besides, the outer oxide layer thickness of the GaN feedstock surface was 1.34 nm. After the cold spray process, the oxide layer thickness formed on the GaN coating surface reached 1.54 nm.

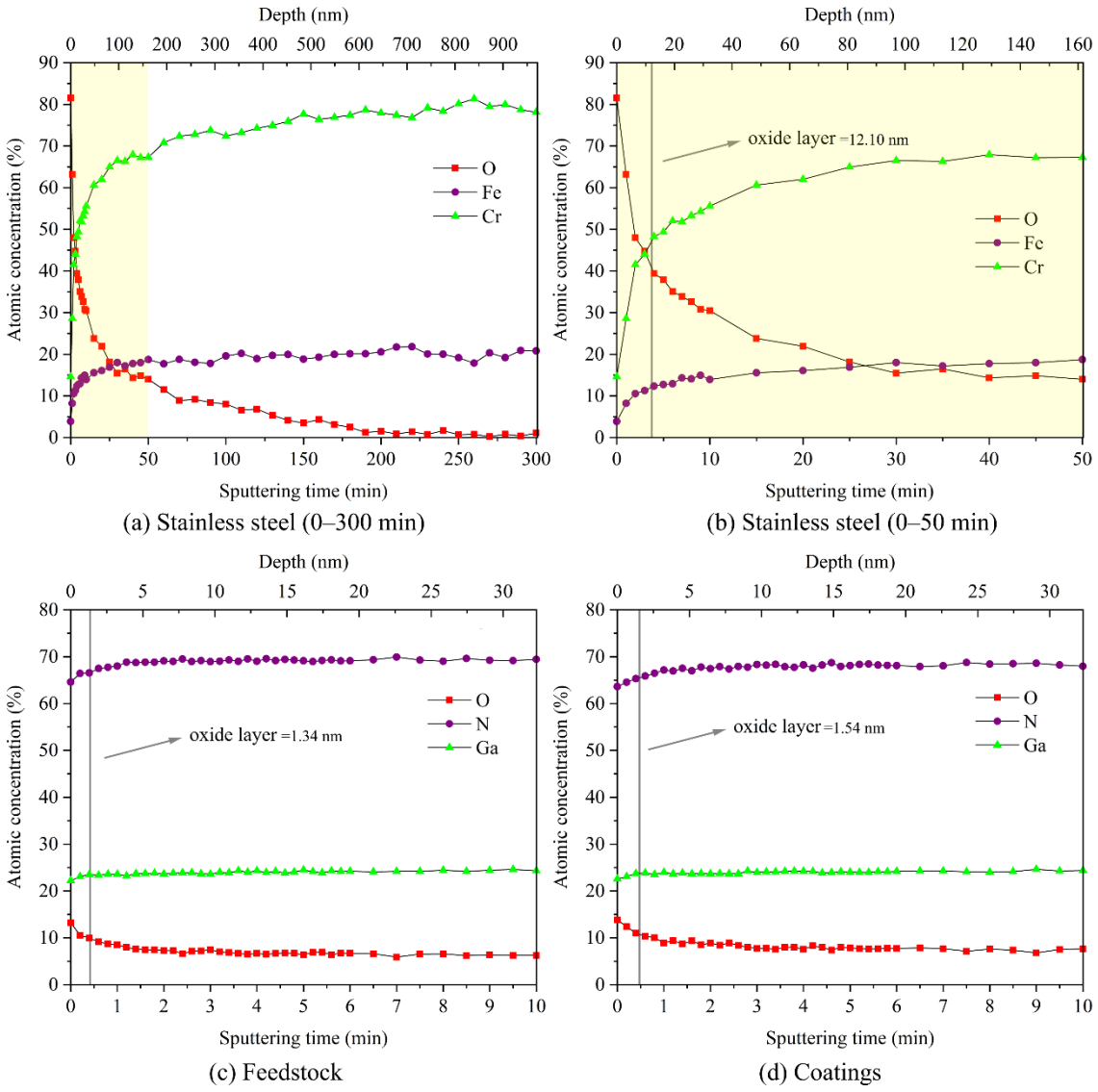

Fig. 4. X-ray photoelectron spectroscopy (XPS) depth profiles of oxide films for (a–b) stainless steel substrates at different sputtering times, (c) GaN feedstock, and (d) cold-sprayed GaN coatings.

As mentioned by Kushvaha et al. [46], the oxide layer measured for the GaN feedstock and at the surface of the GaN coating can be attributed to the formation of a thin Ga_2O_3 film on the coating and particle surface because of their exposure to air. To compare the oxide layer composition of the GaN feedstock surface and cold-sprayed coating surface, Fig. 5 depicts the XPS spectra of O1s for these two samples at different

sputtering times: (i) at 0 min, on the top surface; (ii) at 24 seconds, close to the oxide layer boundary; and (iii) at 6 min, far from the top surface and oxide layer, when all the element contents are in a stable state. Each O1s spectrum was deconvoluted using a Gaussian–Lorentzian distribution function into Ga–O and O vacancies according to their binding energies, as reported in the literature [47–49]. While the peak position remains relatively constant for the feedstock powder, the coating showed a slight shift to the lower binding energy of O1s. It can be attributed to the reduction of oxygen vacancy concentration after cold spray [47,50].

To further examine the difference in Ga–O bond ratio distribution in depth for these two samples, the area ratio of Ga–O bond for each sputtering time is illustrated in Fig. 6, where the remaining ratio belongs to the O vacancies. For both samples, the area ratio of Ga–O bond increased with the sputtering time until 1 minute, before reaching a plateau (see Fig. 6). With the depth increasing, the coating sample exhibited a higher Ga–O bond ratio than the powder sample. It can be attributed to the higher concentration of amorphous oxide compounds in the powder sample that transitioned into gallium oxide with increasing depth after the cold spray process [47,50].

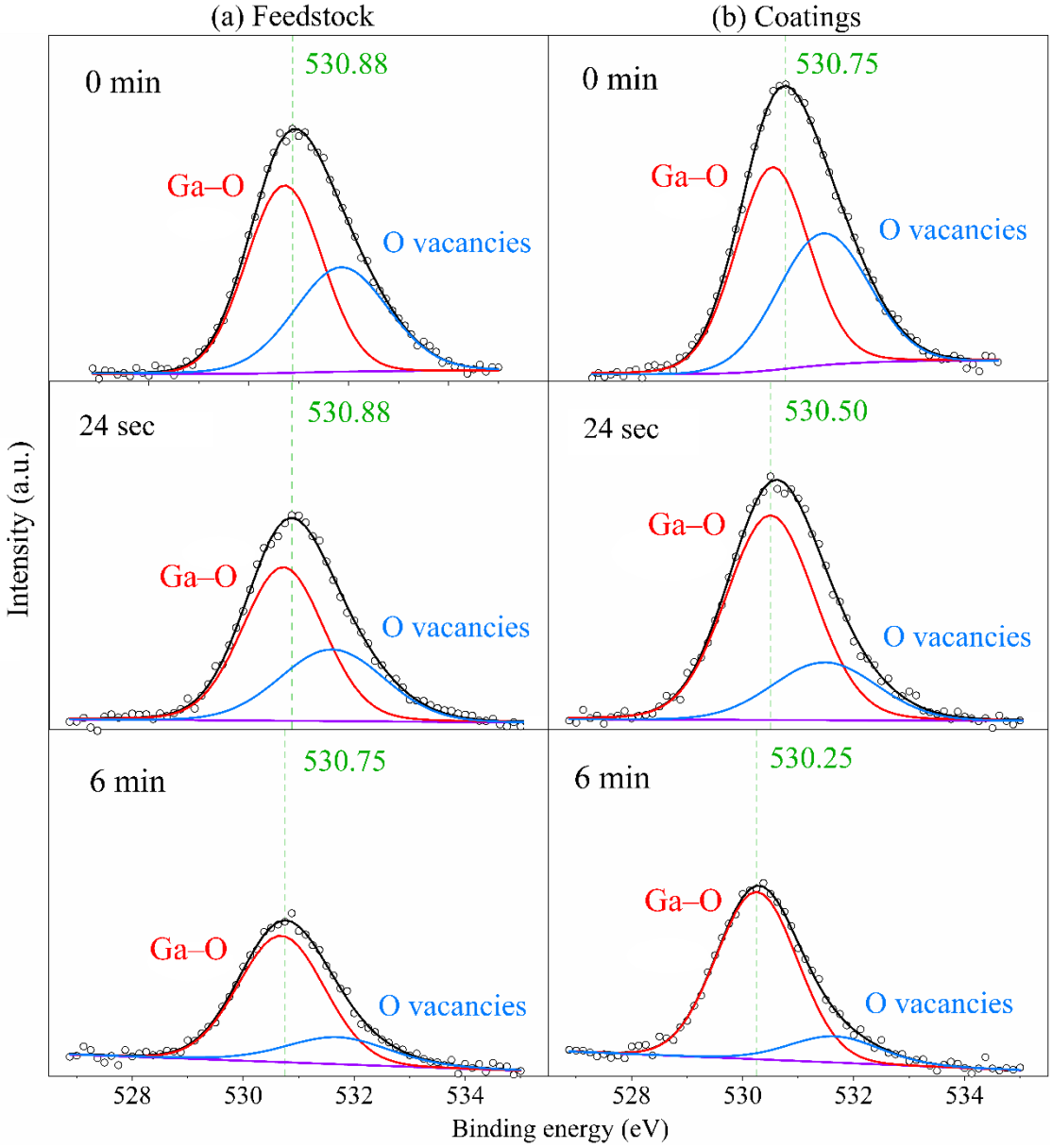

Fig. 5. XPS spectrum of the O1s for (a) GaN feedstock surface and (b) cold-sprayed GaN coating surface at the sputtering times 0 min (top surface), 24 seconds (close to the oxide layer boundary), and 6 min (far from the top surface and oxide layer boundary).

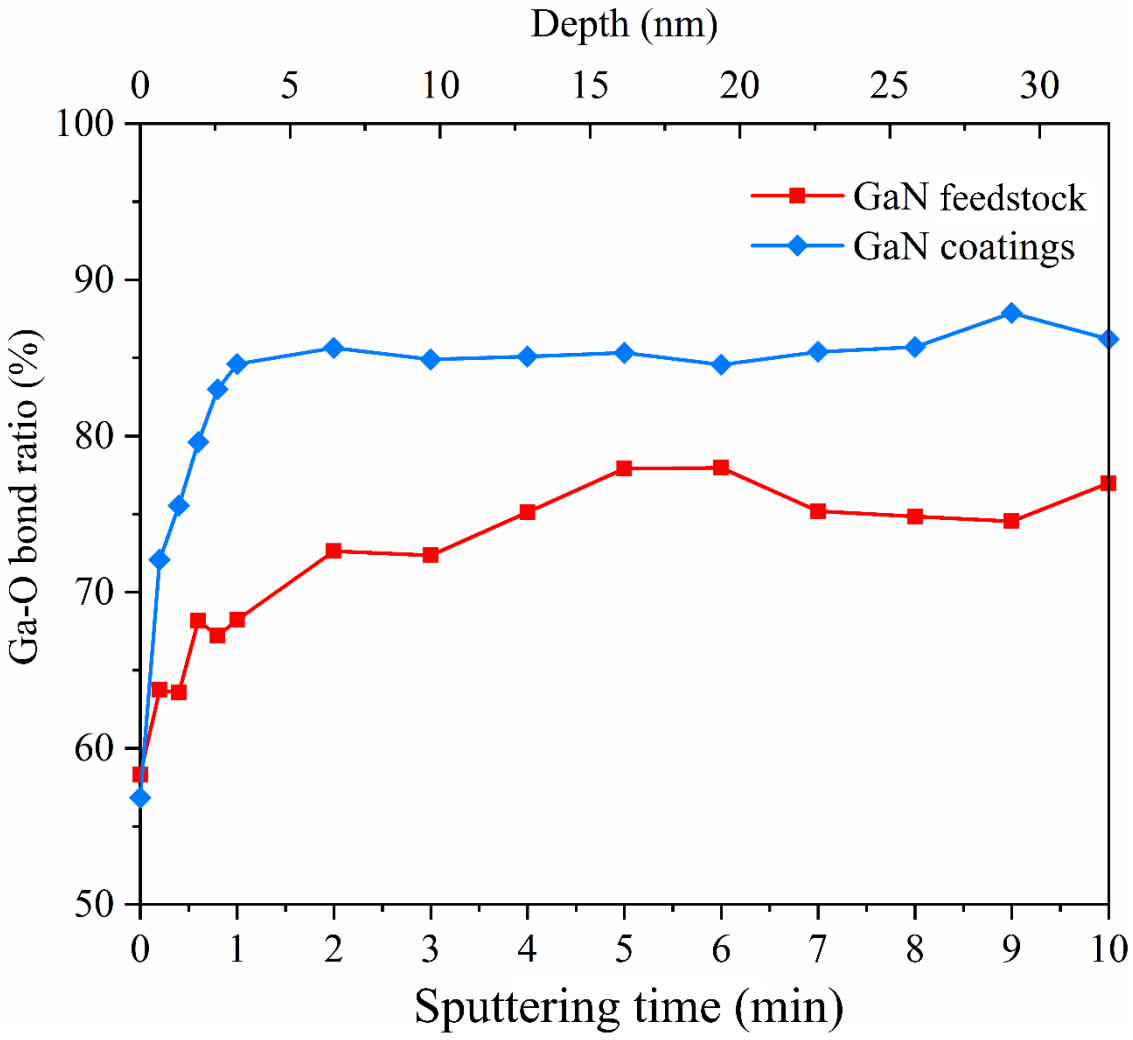

Fig. 6. The area ratio of Ga–O bond at different sputtering times for GaN feedstock and GaN coatings, respectively.

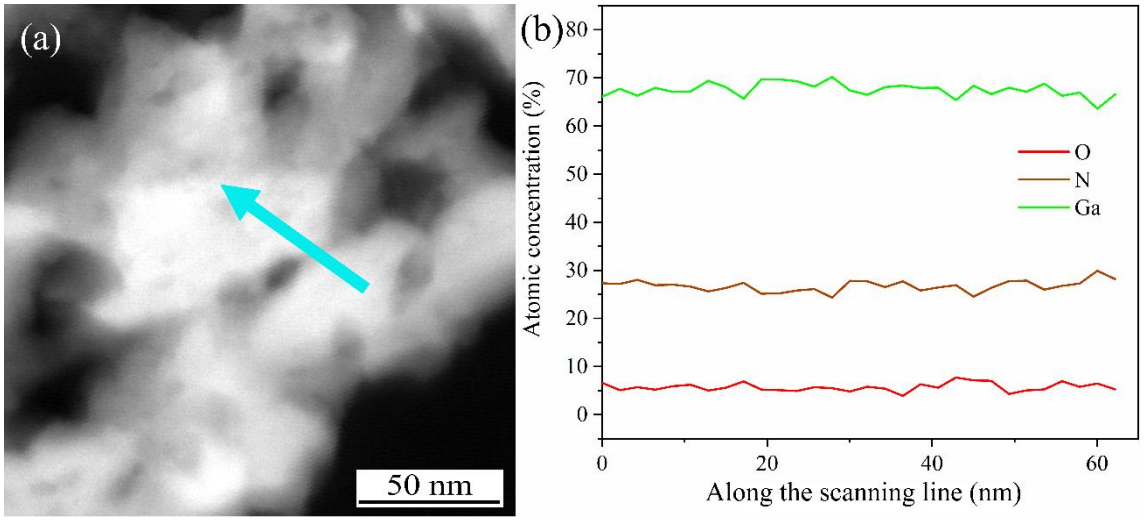

Fig. 7. Characterization of the GaN feedstock oxide layer. (a) HAADF-STEM image and (b) corresponding EDS line scan.

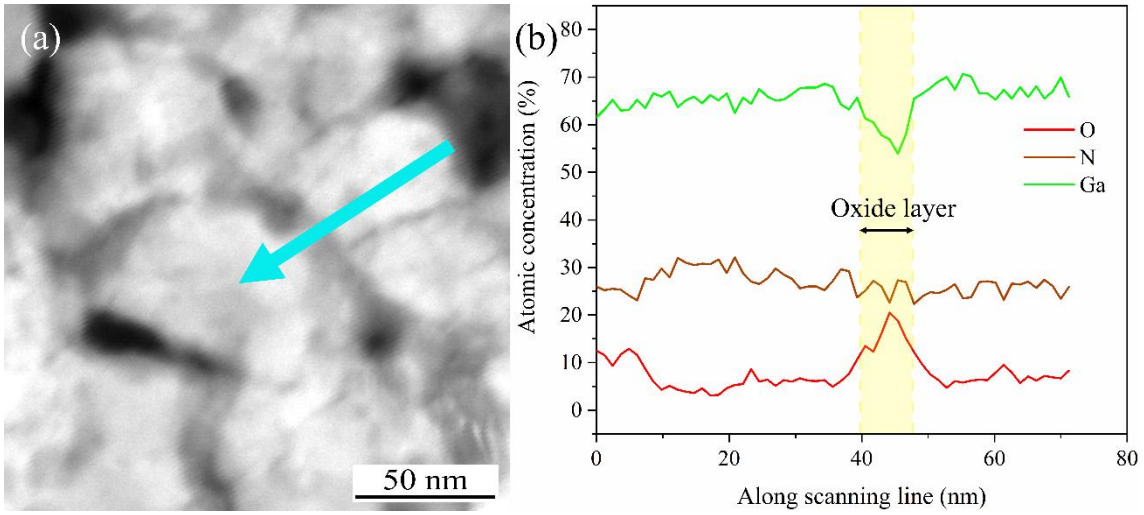

Fig. 8. Characterization of the deposited particles oxide layer (GaN inner coating). (a) HAADF-STEM image and (b) corresponding EDS line scan.

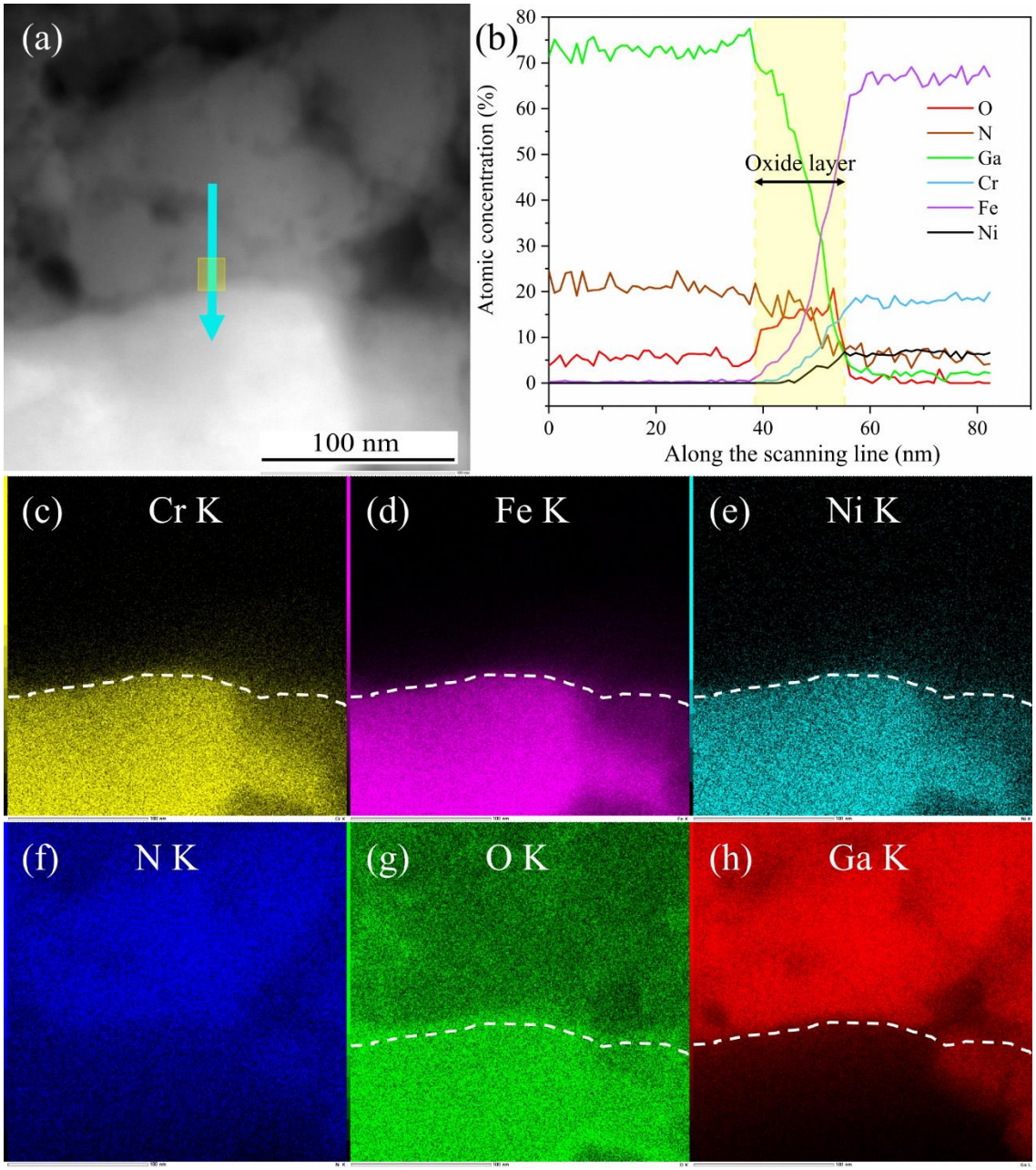

Fig. 9. (a) HAADF-STEM image at the coating/substrate interface, (b) corresponding STEM-EDS line scan, and EDS elemental mapping distributing of (c) Cr K, (d) Fe K, (e) Ni K, (f) N K, (g) O K, and (h) Ga K. The white dashed line corresponds to the interface between the GaN coating and the stainless steel substrate.

HAADF-STEM analysis was conducted to verify the presence of an oxide layer in the inner GaN feedstock and coatings, and, if applicable, to measure the oxide layer

thickness [31]. The corresponding HAADF-STEM-EDS line scan should be detected perpendicularly to the interface between two adjacent nano-sized particles and the particle/substrate interface. Line scanning was performed meticulously to avoid nano-sized porosity. Besides, to minimize the error, line scans were obtained more than three times for each specimen (feedstock, coating, and particle/substrate interface). A typical example of the HAADF-STEM-EDS line scan results is given in Figs. 7 to 9 for the different investigated TEM positions. The oxide layer thickness for the different configurations is summarized in Table 5.

Even though an oxide layer was detected by XPS on the GaN feedstock (agglomerated particles), no oxide layer was detected at the interface between two nano-sized particles by HAADF-STEM-EDS (see Fig. 7b). Thus, the possibility of forming an oxide layer with air within the inner agglomerated particles, which represents most of the feedstock, is limited. However, the XPS results revealed the presence of a thin oxide layer on the surface of the super-agglomerated particles, which could be attributed to the higher possibility to contact with air.

HAADF-STEM-EDS line scanning was performed within the coating thickness to investigate the presence of an oxide layer at the interface between two particles after cold spraying. The results reported in Fig. 8 reveal the presence of an oxide film, approximately 4.20 ± 0.47 nm thick. The thickness was estimated by the FWHM of the O content [28,30,31].

The results of the coating/substrate interface are illustrated in Fig. 9. The HAADF-STEM-EDS line scanning (Fig. 9b) revealed the presence of an oxide layer at the coating/substrate interface (Fig. 9a). Concurrently, Fig. 9c–h illustrates the corresponding EDS mapping for Cr, Fe, Ni, N, O, and Ga elemental intensity distribution, where the

white dashed line corresponds to the interface between GaN coating and stainless steel substrate. The oxide layer, identified by a yellow box in Fig. 9a and b, is 18.14 ± 5.16 nm thick. According to the EDS mapping data for elemental intensity (see Fig. 9b), the oxide layer is mostly distributed in the coating part rather than the substrate part, where high intensity of O and Ga can be observed. Furthermore, the atomic concentrations of O, N, and Ga from the line scan became stable when the scanning position was far from the interface. As the nano-sized particles of the feedstock do not exhibit any oxide layer (see Fig. 7), oxygen diffusion from the coating side does not seem to be a plausible explanation for the presence of an oxide layer at the particle/substrate interface. Instead, a new oxide layer is generated at the substrate/particle interface during the cold spray, probably due to chemical reactions between oxygen and gallium to form gallium oxide. According to the aforementioned experimental work, Table 5 summarizes all the variations of the oxide layer at different positions.

An interpretation of the interfacial oxidation progression is given below. According to the cold spray deposition mechanism for metal materials [8–12], the original oxide layer of the stainless steel 304 substrate would be destroyed and removed on the premise of consecutive bombardment of impacting particles. Simultaneously, a new oxide layer, mainly derived from the chemical reaction between particles and compressive air, is generated near the interface. Moreover, gallium oxide exists in several chemical compositions, including GaO, Ga_2O, and Ga_2O_3. Thus, to further study the oxidation mechanism, the standard free energy of the different oxides was calculated and plotted in Fig.10 as a function of the temperature [51,52]. Considering the porous microstructure of the GaN coating, O_2 may be present in the nano-pores, thereby supporting the chemical reaction at the origin of the oxide film formation.

As shown in Fig. 10, the standard free energy of Ga_2O_3 formation was more negative than that of GaO, and Ga_2O from ambient temperature (300 K) to 700 K [53]. Therefore, the oxide layer, likely originating from the Ga_2O_3 phase during the cold spray, induced interfacial oxidation at the GaN coating/substrate interface.

Table 5

Summary of the oxide layer thickness for the GaN feedstock, substrate, and coatings.

Specimen		Oxide layer thickness (nm)	Method
GaN feedstock	Agglomerates surface	1.34	XPS depth detection
	Nano-sized particles within the agglomerate	No oxide layer detected	STEM line scan
Stainless steel (sandblasted) surface		12.10	XPS depth detection
Deposited coatings	Coating surface	1.54	XPS depth detection
	Deposited particles surface	4.20 ± 0.47	STEM line scan
	Coating/substrate interface	18.14 ± 5.16	STEM line scan

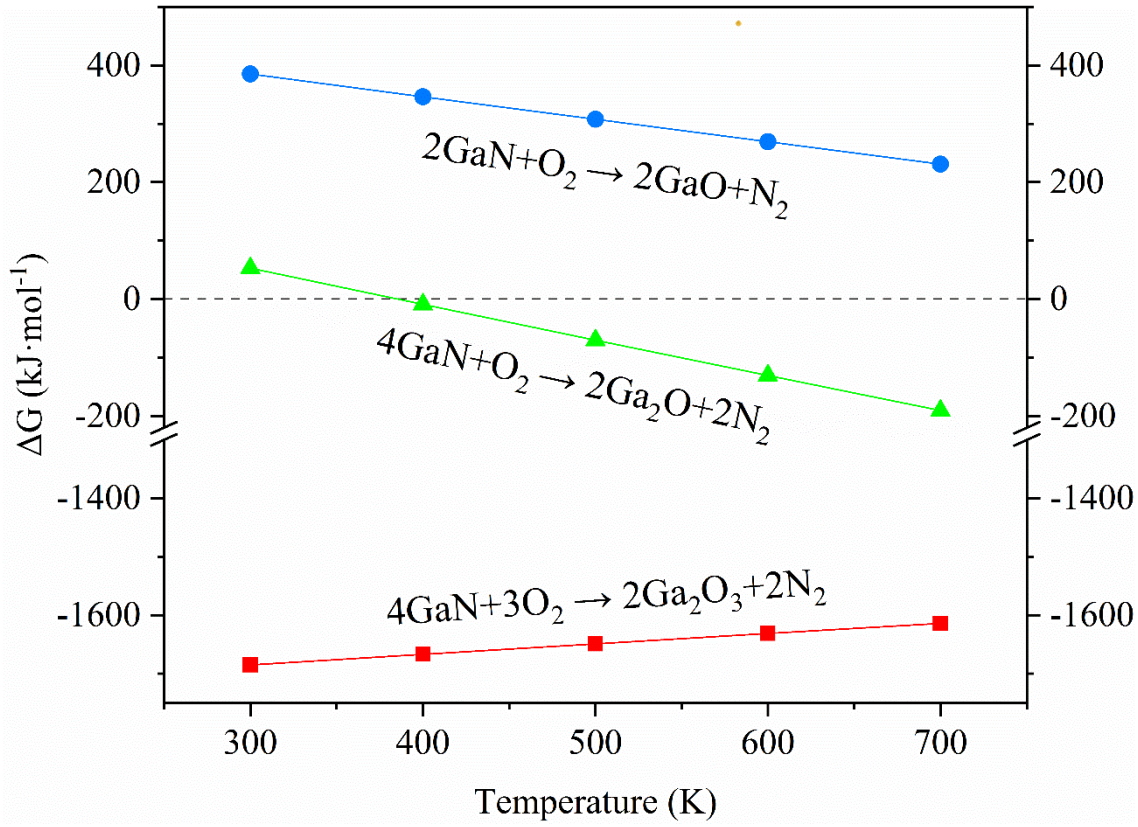

Fig. 10. Evolution of the standard free energy in the formation of the different gallium oxide in the function of temperature.

3.4 Interfacial structures

HRTEM observations were performed to analyze the microstructure of the GaN feedstock, deposited particles, coating interface, and substrate. As displayed in Fig. 11, the HRTEM images and the corresponding FFT patterns were obtained to illustrate the crystallographic characteristics of the hexagonal GaN feedstock [23]. Boxes 1 and 2 illustrate that the GaN (002) plane is close to the particle boundary, and box 3 reveals that the GaN (101) plane is far away from the particle boundary. The selected areas also revealed defect-free and distortion-free crystal fringes in the feedstock particles.

Fig. 12 displays the HRTEM image of the GaN coating located far from the particle/substrate interface. The FFT diffractogram (boxes 1 and 2), close to the

particle/particle interface, revealed diffuse halos, characteristic of the unambiguous presence of an amorphous phase. At a distance away from the particle/particle interface, close to the grain center (boxes 3 and 4), the diffractogram is characteristic of a crystalline GaN (100) plane with $d(100)_{GaN}$ = 0.28 nm.

Meanwhile, boundary amorphization was observed at the particle/substrate interface (Fig. 13). This thin transition zone was highlighted by the corresponding FFT diffractogram of box 3 (see Fig. 13), where only a halo pattern was observed. Combined EDS line scans performed in the STEM mode and analysis of standard free energy (see Figs. 9 and 10) revealed that oxygen mainly originated from Ga_2O_3 formation. The FFT results (box 2) revealed that the lattice planes of trigonal Ga_2O_3 (202) are parallel to the lattice planes of orthorhombic FeNi (002) obtained in box 1, with a corresponding lattice mismatch of only -2.51% [54]. Simultaneously, Ga_2O_3 (204) observed in box 2 is also parallel to GaN (102) obtained in box 4, with lattice mismatch at only -2.65%. The resultant lattice mismatch was deduced based on the Eq. (1) and (2) with the interplanar spacings $d(202)_{Ga_2O_3}$ = 2.04 Å, $d(002)_{FeNi}$ = 1.99 Å, $d(204)_{Ga_2O_3}$ = 1.84 Å, and $d(102)_{GaN}$ = 1.89 Å, respectively [55].

$$\delta 1 = \frac{d(202)_{Ga_2O_3} - d(002)_{FeNi}}{d(002)_{FeNi}} = -2.51\% \quad (1)$$

$$\delta 2 = \frac{d(204)_{Ga_2O_3} - d(102)_{GaN}}{d(102)_{GaN}} = -2.65\% \quad (2)$$

$$\delta 3 = \frac{d(101)_{GaN} - d(111)_{FeNi}}{d(111)_{FeNi}} = 16.02\% \quad (3)$$

The parallel alignment of the GaN (101) from FFT (box 4) and FeNi (111) from box 1 was also observed. Based on the Eq. (3), the corresponding alignment led to an

associated mismatch of 16.02%. Therefore, the particular lattice misfit between GaN and stainless steel is overcome through the newly generated Ga_2O_3 near the interface, which adapts to the lattice of the interface-near metallic surface and ceramic coating [56]. This phenomenon, known as local heteroepitaxy, requires aligned parallel lattice planes and similar interplanar distances [54,55]. The beneficial effect of local heteroepitaxy is demonstrated by the good adhesion between coating and substrate [54,55]. Consequently, according to the local orientation relationship analysis, newly-generated Ga_2O_3 near the GaN/stainless steel interfaces induced partial heteroepitaxy. Therefore, the interlocking between the counterparts is strengthened at the atomic scale.

By comparison, the multiplication of dislocations identified by inverse fast Fourier transform (IFFT) for the dislocation density of box 4 (see Fig. 13) seems rather significant in contrast to the deposited particles far from the interface (Fig. 12, boxes 3 and 4). Accordingly, the dislocations exhibited by the coating should be primarily driven by particle impact during the coating formation stage [57]. This justified the predominant effect of impact-induced deformation on the formation of dislocations.

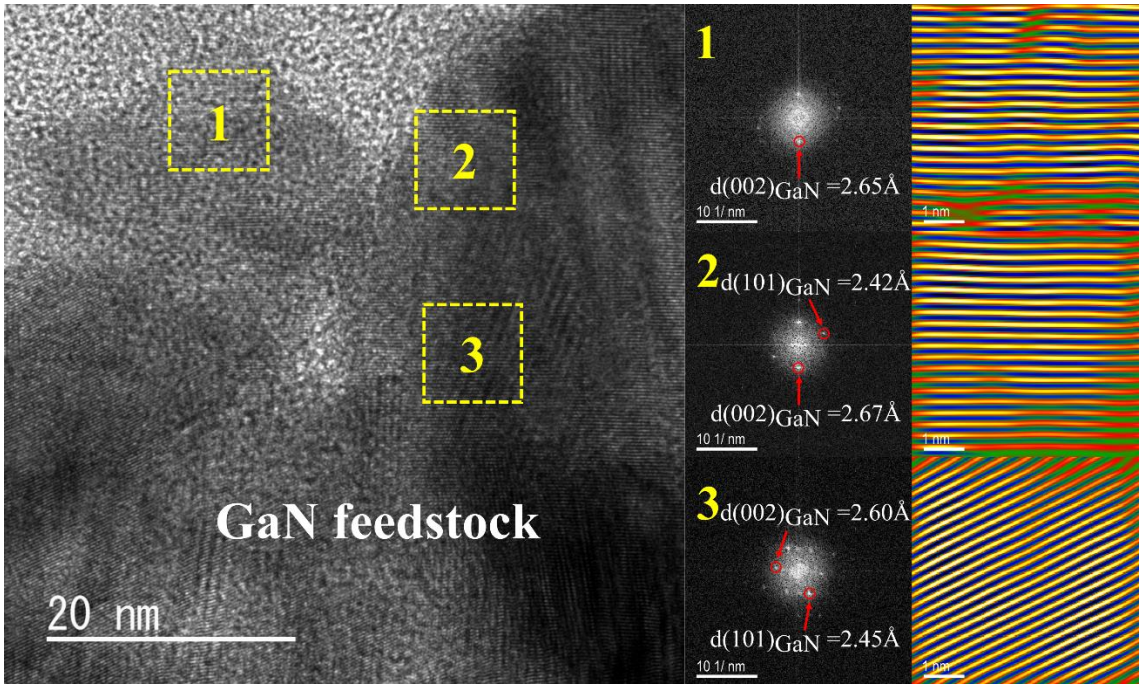

Fig. 11. HRTEM image of the GaN feedstock. The crystallographic orientations of GaN (002) at boxes 1 and 2 were close to the particle boundary, and GaN (101) at box 3 were far from the particle boundary. Both of them exhibit defect-free and distortion-free crystal fringes.

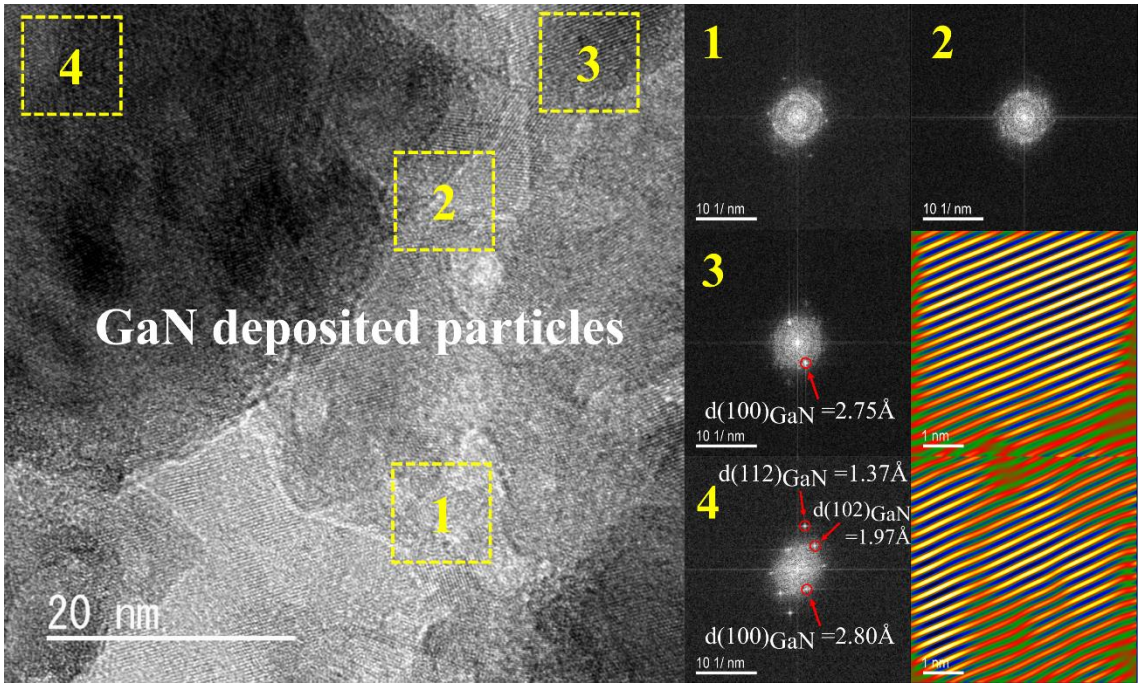

Fig. 12. HRTEM image of GaN coating. The particles are located within the coating far away from the substrate and the coating top surface. On this HRTEM image, four locations were investigated: close to the particle boundary (boxes 1 and 2) and far from the particle boundary (boxes 3 and 4). Boxes 1 and 2 reveal diffuse halos, a characteristic of the amorphous phase layer. Boxes 3 and 4 exhibit crystallographic orientations of GaN (100), with defect-free crystal fringes.

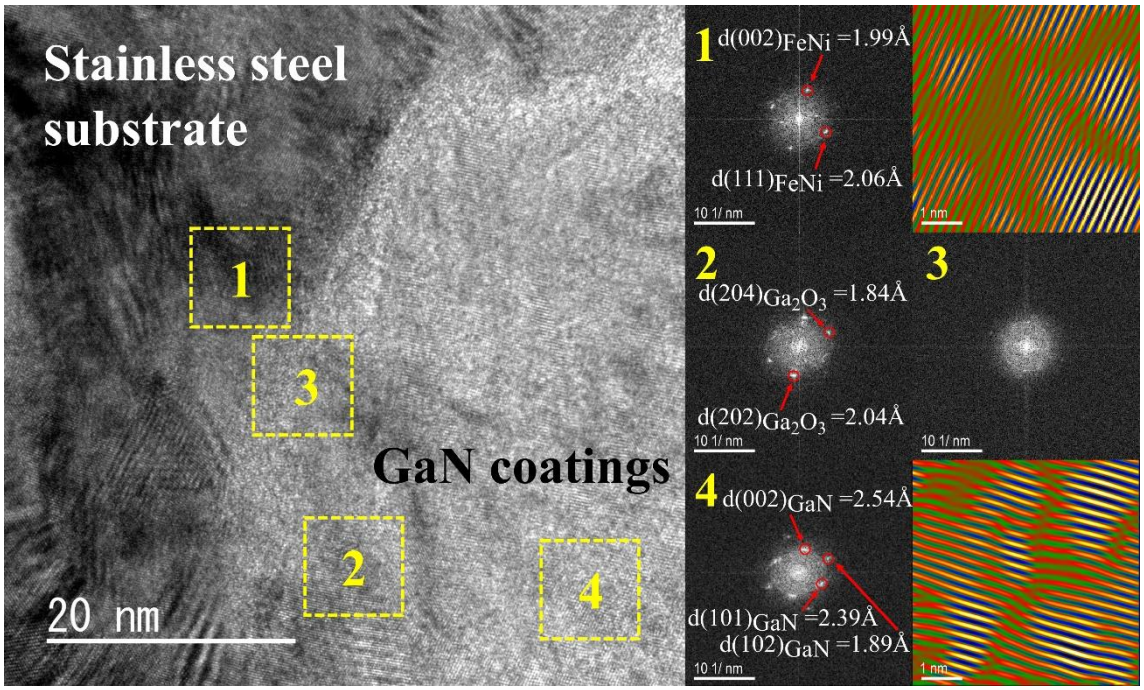

Fig. 13. HRTEM image of particle/substrate interface after cold spray. On this HRTEM image, four locations were investigated: close to the interface (boxes 1, 2, and 3) and far from the interface (box 4). Box 3 illustrates unambiguous amorphization near the interface. Boxes 1, 2, and 3 display the crystallographic orientations of FeNi, Ga_2O_3, and GaN, respectively. Furthermore, the multiplication of dislocations is observed from the IFFT of corresponding boxes 1 and 4.

4. Discussion

The GaN feedstock powder exhibits a complex microstructure: nano-sized particles of 75.9 ± 15.5 nm diameter (Fig.14a) are naturally agglomerated into ellipsoidal micro-sized particles at approximately 1.97 μm in length (Fig.14b). Concurrently, some of these micro-sized particles are themselves agglomerated into super-agglomerated particles of 50–100 μm diameter (see Fig.14c). Based on the above observations, we propose a plausible explanation for the bonding mechanisms of GaN powder on stainless steel substrate, and GaN particle/GaN particle (see Fig.14). The deposition mechanism of the first layer was driven by the mechanical interlocking.

Relatively rough substrate surface provides a higher contact area, thereby improving the adhesion between the ceramic and metals [33,34]. Concurrently, mechanical interlocking involves the fragmentation of agglomerated particles and shock compaction of the nano-sized particles. The ambiguous particle boundaries observed within the coatings further confirm this phenomenon. Specifically, micro-sized and super-agglomerated particles strike on the substrate, therefore, fragmentation and packing occur (Fig. 14e) [58]. With the successive impacts of the following particles striking the accumulated nanoparticles, the nano-sized particles are effectively compacted at high heat energy and pressure [14,37]. Therefore, weak adhesion was facilitated, which resulted in few bonding sites, consequently leading to consistent and consolidated layers with ambiguous particle boundaries (Fig. 14f) [59].

Due to the size effect of the ductile-brittle transition, the nano-sized GaN particles did not undergo severe fragmentation [43–45]. The impacted nano-sized particles remain at around 70 nm diameter (Fig. 14h), therefore, grain refinement was not necessary for the brittle particle deformation during the cold spray process. Furthermore, the presence

of nano-pores inside the coatings provides O_2 for the chemical reaction into oxide compounds. While no oxide film was detected on nano-sized particles by TEM, XPS results demonstrated the presence of a 1.34 nm thick oxide film in the GaN feedstock, which was assimilated to the oxide layer of super-agglomerated particles.

For metal materials during the cold spray process, the original oxide layer would be broken and removed by the plastic deformation of metals near the surface [8,34]. Therefore, the oxide layer originating from the stainless steel 304 substrate could be destroyed by sufficient impact during the cold spray (Fig. 14i). Besides, successive particle impact is considerably important for strong bonding as they provide heat and pressure in the form of impact energy [58]. Concurrently, a newly generated oxide layer, 18.14 ± 5.16 nm thick, was observed at the coating/substrate interface (see Fig. 14i). This oxide layer, mainly distributed within the coating, is considerably thicker than the one measured in the GaN feedstock.

HRTEM characterization of the feedstock powder revealed defect-free crystal fringes, whereas the boundary at the places in vicinal deposited particle edges and the coating interface indicated the presence of an amorphous phase. Meanwhile, near the deposited particle/substrate interface, an increase in the dislocation density is observed. According to Ko et al. [60] and Balani et al. [61], and based on the TEM observations, the dislocations were driven by the severe particle impact induced by the cold spraying. Near the particle/substrate interface, aligned parallel lattice planes and similar interplanar distances resulted in a low lattice mismatch with the formation of gallium oxide (Ga_2O_3). Thus, the presence of a local heteroepitaxy that facilitates the adhesion between GaN particles and stainless steel substrates was revealed.

If the oxide layer is believed to act as a restriction to metallurgical bonding for metal-to-metal contact by cold spray [12], the oxide layer at the ceramic particle/metallic substrate interface might not be an obstacle. Thus, interfacial oxidation might be a critical factor that influences the bonding between the ceramic particles and the metallic substrate.

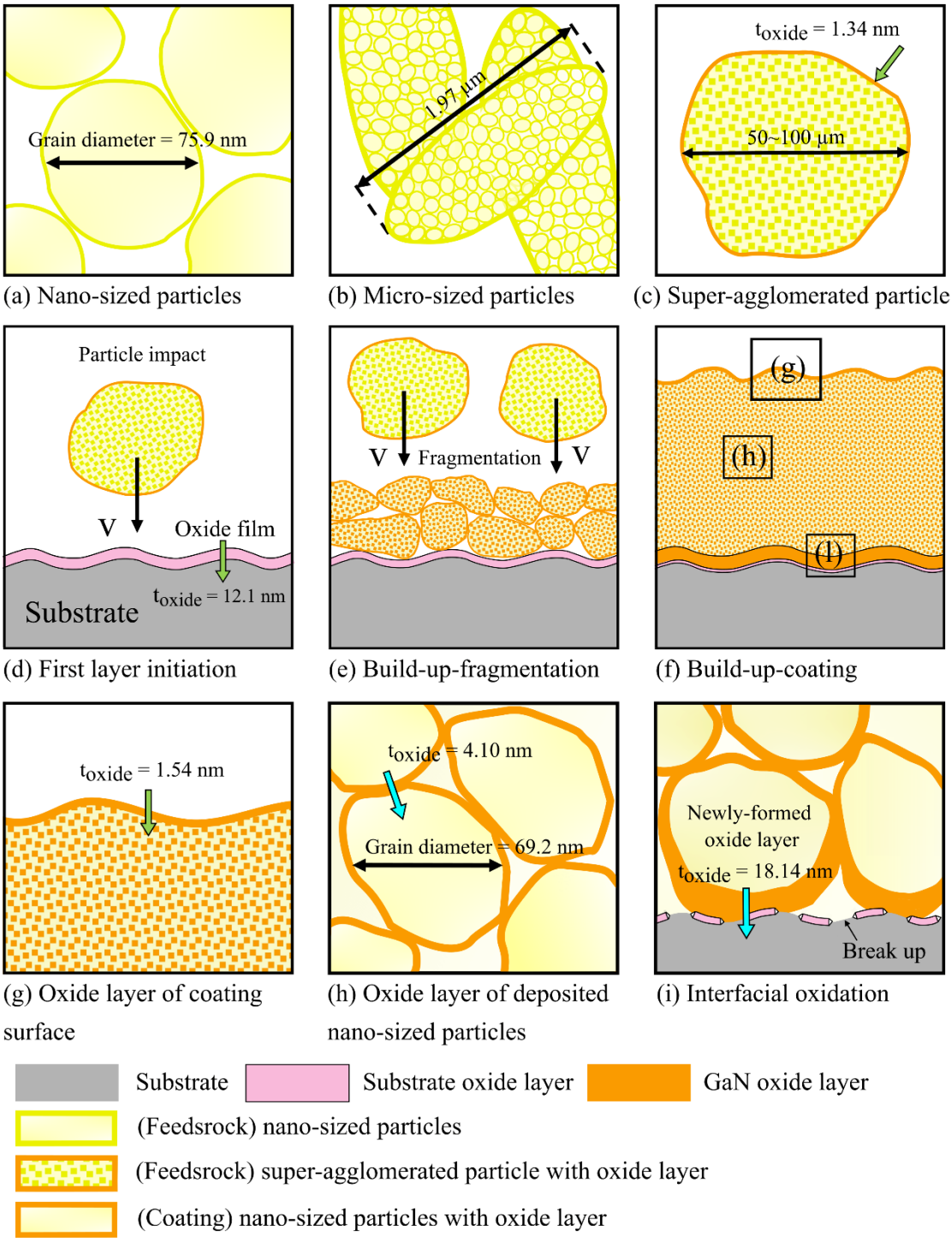

Fig. 14. Bonding mechanism of GaN particles impacted under stainless steel 304 substrates, (a) Nano-sized particles, (b) micro-sized particles, (c) super-agglomerated particle, (d) first layer initiation, (e) build-up-fragmentation, (f) build-up-coating, (g)

oxide layer on the coating surface, (h) oxide layer on the deposited nano-sized particles, and (i) interfacial oxidation.

5. Conclusion

In this study, cold sprayed GaN coatings onto stainless steel 304 substrates were developed to elucidate the deposition mechanism between nitride ceramic particles and metallic substrate. The following conclusions were obtained:

i. The coating is formed through severe fragmentation and coordinated deformation of the micro-sized agglomerated and super-agglomerated particles, leading to strong particle/particle bonding. Moreover, compared with as-received substrates, sandblasted substrates possess a relatively rough substrate surface, which facilitates the mechanical interlocking for the first layer formation.

ii. No indication of significant fragmentation was found for nano-sized particles, which remain around 70 nm from feedstock to coatings. These facts revealed that grain refinement is not the key factor affecting the deposition mechanism of brittle particles by cold spray.

iii. Before cold spray, the original oxide layer thickness of the feedstock powder is rather insignificant, and the stainless steel substrate surface exhibits a 12.10 nm thick oxide layer. Subsequently, the oxide layer thickness of inner deposited GaN particles is approximately 4.20 ± 0.47 nm after cold spray. Crucially, the original oxide layer on the stainless steel 304 substrate was drastically damaged by the successive impacts exerted by the GaN particles. Meanwhile, a new oxide layer, around 18.14 nm thick, is formed at the coating/substrate interface, proven to be majorly Ga_2O_3.

iv. According to the high-resolution transmission electron microscopy (HRTEM) characterization, localized amorphization was revealed near the particle/particle boundaries and particle/substrate interface. The domains located relatively far from the particle/particle and particle/substrate interfaces in the coating sample, as well as the nano-sized GaN feedstock, exhibited defect-free crystal fringes. In contrast, a high density of dislocations is displayed close to the interface regions. Therefore, high strain rates induced the formation of amorphous structures at their fringes and a relatively high density of dislocations.

v. Local heteroepitaxy between the GaN and stainless steel was observed and is regarded as a critical factor that promotes the adhesion of the coatings.

Based on these conclusions, these novel findings may provide evidence for GaN–metal joints. Moreover, the proposed method to explain the mechanism may be extended to other ceramic–metal combinations and subsequently provide effective methods for adhesion between them.

Declaration of Competing Interest

The authors declare that they have no known competing financial interests or personal relationships that could have appeared to influence the work reported in this paper.

Acknowledgments

This work was supported by the “GP-Mech” (Tohoku University Graduate Program for Integration of Mechanical Systems) program and JST’s “Next Generation Researcher Challenging Research Support Project”. The authors would like to acknowledge Mr. Masatoshi Tanno from Tohoku University for his support in performing the XPS

measurements. Also, Shaoyun Zhou would like to acknowledge Dr. Zihao Wang and Dr. Yi Shuang from Tohoku University for the fruitful discussions. Their help is highly appreciated.

References

[1] Y. Xie, S. Yin, C. Chen, M.P. Planche, H. Liao, R. Lupoi, New insights into the coating/substrate interfacial bonding mechanism in cold spray, Scr. Mater. 125 (2016) 1–4. https://doi.org/10.1016/j.scriptamat.2016.07.024.

[2] L. He, D.C. Pagan, A. Nardi, M. Hassani, Synchrotron X-ray diffraction studies of the phase-specific deformation in additively manufactured Ni–CrC composites, Compos. Part B Eng. 222 (2021) 109086. https://doi.org/10.1016/J.COMPOSITESB.2021.109086.

[3] J. Sun, S. Zhou, K. Yamanaka, Y. Ichikawa, H. Saito, K. Ogawa, A. Chiba, Thermal effects in Sn coating on a carbon fiber reinforced plastic by cold spraying, J. Therm. Spray Technol. 305 (2021) 1254–1261. https://doi.org/10.1007/S11666-021-01208-9.

[4] Y. Zou, Cold spray additive manufacturing: microstructure evolution and bonding features, Acc. Mater. Res. 2 (2021) 1071–1081. https://doi.org/10.1021/ACCOUNTSMR.1C00138.

[5] R.N. Raoelison, Y. Xie, T. Sapanathan, M.P. Planche, R. Kromer, S. Costil, C. Langlade, Cold gas dynamic spray technology: a comprehensive review of processing conditions for various technological developments till to date, Addit. Manuf. 19 (2018) 134–159. https://doi.org/10.1016/J.ADDMA.2017.07.001.

[6] A. Moridi, S.M. Hassani-Gangaraj, M. Guagliano, M. Dao, Cold spray coating: review of material systems and future perspectives, Surf. Eng. 30 (2014) 369–395. https://doi.org/10.1179/1743294414Y.0000000270.

[7] N. ul, H. Tariq, L. Gyansah, X. Qiu, C. Jia, H. Bin Awais, C. Zheng, H. Du, J. Wang, T. Xiong, Achieving strength-ductility synergy in cold spray additively manufactured Al/B4C composites through a hybrid post-deposition treatment, J. Mater. Sci. Technol. 35 (2019) 1053–1063. https://doi.org/10.1016/J.JMST.2018.12.022.

[8] Y. Ichikawa, R. Tokoro, M. Tanno, K. Ogawa, Elucidation of cold-spray deposition mechanism by auger electron spectroscopic evaluation of bonding interface oxide film, Acta Mater. 164 (2019) 39–49. https://doi.org/10.1016/j.actamat.2018.09.041.

[9] S. Yin, M. Hassani, Q. Xie, R. Lupoi, Unravelling the deposition mechanism of brittle particles in metal matrix composites fabricated via cold spray additive manufacturing, Scr. Mater. 194 (2021) 113614. https://doi.org/10.1016/J.SCRIPTAMAT.2020.10.055.

[10] G. Bae, S. Kumar, S. Yoon, K. Kang, H. Na, H.J. Kim, C. Lee, Bonding features and associated mechanisms in kinetic sprayed titanium coatings, Acta Mater. 57 (2009) 5654–5666. https://doi.org/10.1016/j.actamat.2009.07.061.

[11] Y. Ichikawa, K. Ogawa, Effect of substrate surface oxide film thickness on deposition behavior and deposition efficiency in the cold spray process, J. Therm. Spray Technol. 24 (2015) 1269–1276. https://doi.org/10.1007/s11666-015-0299-y.

[12] J. Lienhard, C. Crook, M.Z. Azar, M. Hassani, D.R. Mumm, D. Veysset, D. Apelian, K.A. Nelson, V. Champagne, A. Nardi, C.A. Schuh, L. Valdevit, Surface oxide and hydroxide effects on aluminum microparticle impact bonding, Acta Mater. 197 (2020) 28–39. https://doi.org/10.1016/J.ACTAMAT.2020.07.011.

[13] W. Li, H. Assadi, F. Gaertner, S. Yin, A review of advanced composite and nanostructured coatings by solid-state cold spraying process, Crit. Rev. Solid State Mater. Sci. 44 (2018) 109–156. https://doi.org/10.1080/10408436.2017.1410778.

[14] L.S. Wang, H.F. Zhou, K.J. Zhang, Y.Y. Wang, C.X. Li, X.T. Luo, G.J. Yang, C.J. Li, Effect of the powder particle structure and substrate hardness during vacuum cold spraying of Al_2O_3, Ceram. Int. 43 (2017) 4390–4398. https://doi.org/10.1016/J.CERAMINT.2016.12.085.

[15] F. Cao, H. Park, G. Bae, J. Heo, C. Lee, Microstructure evolution of titanium nitride film during vacuum kinetic spraying, J. Am. Ceram. Soc. 96 (2013) 40–43. https://doi.org/10.1111/JACE.12101.

[16] A.R. Toibah, M. Sato, M. Yamada, M. Fukumoto, Cold-sprayed TiO_2 coatings from nanostructured ceramic agglomerated powders, Mater. Manuf. Process. 31 (2016) 1527–1534. https://doi.org/10.1080/10426914.2015.1090587.

[17] L. Pawlowski, Finely grained nanometric and submicrometric coatings by thermal spraying: a review, Surf. Coatings Technol. 202 (2008) 4318–4328. https://doi.org/10.1016/J.SURFCOAT.2008.04.004.

[18] H. Park, J. Kwon, I. Lee, C. Lee, Shock-induced plasticity and fragmentation

phenomena during alumina deposition in the vacuum kinetic spraying process, Scr. Mater. 100 (2015) 44–47. https://doi.org/10.1016/J.SCRIPTAMAT.2014.12.008.

[19] J. Akedo, Room temperature impact consolidation and application to ceramic coatings: aerosol deposition method, J. Ceram. Soc. Japan. 128 (2020) 101–116. https://doi.org/10.2109/JCERSJ2.19196.

[20] M. Winnicki, A. Baszczuk, M. Jasiorski, B. Borak, A. Małachowska, Preliminary studies of TiO_2 nanopowder deposition onto metallic substrate by low pressure cold spraying, Surf. Coatings Technol. 371 (2019) 194–202. https://doi.org/10.1016/J.SURFCOAT.2018.09.057.

[21] N.T. Salim, M. Yamada, H. Nakano, K. Shima, H. Isago, M. Fukumoto, The effect of post-treatments on the powder morphology of titanium dioxide (TiO_2) powders synthesized for cold spray, Surf. Coatings Technol. 206 (2011) 366–371. https://doi.org/10.1016/j.surfcoat.2011.07.030.

[22] T.A. Rahim, K. Takahashi, M. Yamada, M. Fukumoto, Effect of Powder Calcination on the Cold Spray Titanium Dioxide Coating, Mater. Trans. 57 (2016) 1345–1350. https://doi.org/10.2320/MATERTRANS.T-M2016817.

[23] S. Zhou, C.A. Bernard, K. Ravi, H. Saito, Y. Ichikawa, K. Ogawa, S. Yin, Development and characterization of photocatalytic GaN coatings by cold spray process, J. Therm. Spray Technol. 305 (2021) 1294–1309. https://doi.org/10.1007/S11666-021-01207-W.

[24] S. Zhou, C.A. Bernard, K. Ravi, Y. Ichikawa, K. Ogawa, The feasibility study of GaN coatings by cold spray technique, in: Proceedings of the International

Thermal Spray Conference and Exposition, ITSC 2019, Yokohama, Japan, 2019, pp. 462–468. https://doi.org/10.2/JQUERY.MIN.JS.

[25] R.N. Raoelison, Y. Xie, T. Sapanathan, M.P. Planche, R. Kromer, S. Costil, C. Langlade, Cold gas dynamic spray technology: A comprehensive review of processing conditions for various technological developments till to date, Addit. Manuf. 19 (2018) 134–159. https://doi.org/10.1016/J.ADDMA.2017.07.001.

[26] D. Hanft, J. Exner, M. Schubert, T. Stöcker, P. Fuierer, R. Moos, An overview of the aerosol deposition method: process fundamentals and new trends in materials applications, J. Ceram. Sci. Technol. 6 (2015) 147–181. https://doi.org/10.4416/JCST2015-00018.

[27] K. Ravi, W.L. Sulen, C. Bernard, Y. Ichikawa, K. Ogawa, Fabrication of micro-/nano-structured super-hydrophobic fluorinated polymer coatings by cold-spray, Surf. Coatings Technol. 373 (2019) 17–24. https://doi.org/10.1016/j.surfcoat.2019.05.078.

[28] Y. Xiong, Y. Watanabe, Y. Shibayama, N. Mary, Effects of 100 ppb dissolved oxygen on low-cycle fatigue behaviors of 316LN austenitic stainless steel in borated and lithiated high temperature water and mechanism behind these effects, Corros. Sci. 168 (2020) 108567. https://doi.org/10.1016/J.CORSCI.2020.108567.

[29] R. Huang, T. Liu, Y. Zhao, Y. Zhu, Z. Huang, F. Li, J. Liu, L. Zhang, S. Zhang, A. Dingsun, H. Yang, Angular dependent XPS study of surface band bending on Ga-polar n-GaN, Appl. Surf. Sci. 440 (2018) 637–642. https://doi.org/10.1016/J.APSUSC.2018.01.196.

[30] Z. Wang, Y. Takeda, Mechanistic understanding of the roles of hydrogen in

modification of oxide film of alloy 600 in high temperature high pressure water environment, Corros. Sci. 170 (2020) 108656. https://doi.org/10.1016/J.CORSCI.2020.108656.

[31] Z. Wang, Y. Takeda, Roles of permeated hydrogen in the oxidation process of Ni-based alloy in high temperature water environment, Corros. Sci. 179 (2021) 109139. https://doi.org/10.1016/J.CORSCI.2020.109139.

[32] Y. Shuang, S. Hatayama, Y. Saito, P. Fons, A.V. Kolobov, D. Ando, Y. Sutou, Evolution of the local structure surrounding nitrogen atoms upon the amorphous to crystalline phase transition in nitrogen-doped Cr2Ge2Te6 phase-change material, Appl. Surf. Sci. 556 (2021) 149760. https://doi.org/10.1016/J.APSUSC.2021.149760.

[33] N.I. Omar, M. Yamada, T. Yasui, M. Fukumoto, Bonding mechanism of cold-sprayed TiO_2 coatings on copper and aluminum substrates, Coatings 11 (2021) 1349. https://doi.org/10.3390/COATINGS11111349.

[34] J. Sun, K. Yamanaka, S. Zhou, H. Saito, Y. Ichikawa, K. Ogawa, A. Chiba, Adhesion mechanism of Sn coatings on the carbon fiber reinforced plastics using cold spray technique, Appl. Surf. Sci. 79 (2021) 151873. https://doi.org/10.1016/J.APSUSC.2021.151873.

[35] P.H. Gao, Y.G. Li, C.J. Li, G.J. Yang, C.X. Li, Influence of powder porous structure on the deposition behavior of cold-sprayed WC-12Co coatings, J. Therm. Spray Technol. 17 (2008) 742–749. https://doi.org/10.1007/s11666-008-9258-1.

[36] S.Q. Fan, C.J. Li, G.J. Yang, L.Z. Zhang, J.C. Gao, Y.X. Xi, Fabrication of nano-

Tio_2 coating for dye-sensitized solar cell by vacuum cold spraying at room temperature, J. Therm. Spray Technol. 16 (2007) 893–897. https://doi.org/10.1007/S11666-007-9090-Z/FIGURES/5.

[37] J. Kim, J.I. Lee, D.S. Park, E.S. Park, Enhancement of interface anchoring and densification of Y_2O_3 coating by metal substrate manipulation in aerosol deposition process, J. Appl. Phys. 117 (2015) 014903. https://doi.org/10.1063/1.4905241.

[38] R.E. Dunin-Borkowski, The development of Fresnel contrast analysis, and the interpretation of mean inner potential profiles at interfaces, Ultramicroscopy 83 (2000) 193–216. https://doi.org/10.1016/S0304-3991(00)00015-2.

[39] J. Ângelo, L. Andrade, L.M. Madeira, A. Mendes, An overview of photocatalysis phenomena applied to NOx abatement, J. Environ. Manage. 129 (2013) 522–539. https://doi.org/10.1016/j.jenvman.2013.08.006.

[40] Y. Liu, Y. Wang, X. Suo, Y. Gong, C.J. Li, H. Li, Impact-induced bonding and boundary amorphization of TiN ceramic particles during room temperature vacuum cold spray deposition, Ceram. Int. 42 (2016) 1640–1647. https://doi.org/10.1016/J.CERAMINT.2015.09.116.

[41] C.M. Parish, M.K. Miller, Aberration-corrected X-ray spectrum imaging and fresnel contrast to differentiate nanoclusters and cavities in helium-irradiated alloy 14YWT, Microsc. Microanal. 20 (2014) 613–626. https://doi.org/10.1017/S1431927614000312.

[42] L.C. Peng, Y. Zhang, S.L. Zuo, M. He, J.W. Cai, S.G. Wang, H.X. Wei, J.Q. Li, T.Y. Zhao, B.G. Shen, Lorentz transmission electron microscopy studies on

topological magnetic domains, Chin. Phys. B. 27 (2018) 066802. https://doi.org/10.1088/1674-1056/27/6/066802.

[43] S. Kuroyanagi, K. Shinoda, A. Yumoto, J. Akedo, Size-dependent quasi Brittle-Ductile transition of single crystalline alpha-alumina particles during microcompression tests, Acta Mater. 195 (2020) 588–596. https://doi.org/10.1016/J.ACTAMAT.2020.05.065.

[44] I. Issa, J. Amodeo, J. Réthoré, L. Joly-Pottuz, C. Esnouf, J. Morthomas, M. Perez, J. Chevalier, K. Masenelli-Varlot, In situ investigation of MgO nanocube deformation at room temperature, Acta Mater. 86 (2015) 295–304. https://doi.org/10.1016/J.ACTAMAT.2014.12.001.

[45] E. Calvié, J. Réthoré, L. Joly-Pottuz, S. Meille, J. Chevalier, V. Garnier, Y. Jorand, C. Esnouf, T. Epicier, J.B. Quirk, K. Masenelli-Varlot, Mechanical behavior law of ceramic nanoparticles from transmission electron microscopy in situ nano-compression tests, Mater. Lett. 119 (2014) 107–110. https://doi.org/10.1016/J.MATLET.2014.01.002.

[46] S.S. Kushvaha, M. Senthil Kumar, A.K. Shukla, B.S. Yadav, D.K. Singh, M. Jewariya, S.R. Ragam, K.K. Maurya, Structural, optical and electronic properties of homoepitaxial GaN nanowalls grown on GaN template by laser molecular beam epitaxy, RSC Adv. 5 (2015) 87818–87830. https://doi.org/10.1039/C5RA11361J.

[47] P. Li, H. Shi, K. Chen, D. Guo, W. Cui, Y. Zhi, S. Wang, Z. Wu, Z. Chen, W. Tang, Construction of GaN/Ga_2O_3 p-n junction for an extremely high responsivity self-powered UV photodetector, J. Mater. Chem. C. 5 (2017)

10562–10570. https://doi.org/10.1039/c7tc03746e.

[48] NIST XPS Database Detail Page, (n.d.). https://srdata.nist.gov/xps/XPSDetailPage.aspx?AllDataNo=22176 (accessed March 1, 2021).

[49] D.Y. Guo, Z.P. Wu, Y.H. An, X.C. Guo, X.L. Chu, C.L. Sun, L.H. Li, P.G. Li, W.H. Tang, Oxygen vacancy tuned Ohmic-Schottky conversion for enhanced performance in β-Ga_2O_3 solar-blind ultraviolet photodetectors, Appl. Phys. Lett. 105 (2014) 023507. https://doi.org/10.1063/1.4890524.

[50] L. Dong, R. Jia, B. Xin, B. Peng, Y. Zhang, Effects of oxygen vacancies on the structural and optical properties of β-Ga_2O_3, Sci. Rep. 71 (2017) 1–12. https://doi.org/10.1038/srep40160.

[51] I. Barin, Thermochemical Data of Pure Substances, third ed., Wiley, 1995. https://doi.org/10.1002/9783527619825.

[52] H. Lin, W. Liang, Q. Miao, S. Li, Z. Ding, S. Cui, J. Yi, Y. Qi, Z. Yang, H. Yu, Constructing self-supplying Al_2O_3-Y_2O_3 coating for the γ-TiAl alloy with enhanced oxidation protective ability, Appl. Surf. Sci. 522 (2020) 146439. https://doi.org/10.1016/J.APSUSC.2020.146439.

[53] W.S. Jung, H.U. Joo, B.K. Min, Growth of β-gallium oxide nanostructures by the thermal annealing of compacted gallium nitride powder, Physica E Low-Dimens. Syst. Nanostruct. 36 (2007) 226–230. https://doi.org/10.1016/J.PHYSE.2006.12.001.

[54] R. Drehmann, T. Grund, T. Lampke, B. Wielage, K. Manygoats, T. Schucknecht,

D. Rafaja, Interface characterization and bonding mechanisms of cold gas-sprayed Al coatings on ceramic substrates, J. Therm. Spray Technol. 24 (2014) 92–99. https://doi.org/10.1007/S11666-014-0189-8/FIGURES/11.

[55] C. Wüstefeld, D. Rafaja, M. Motylenko, C. Ullrich, R. Drehmann, T. Grund, T. Lampke, B. Wielage, Local heteroepitaxy as an adhesion mechanism in aluminium coatings cold gas sprayed on AlN substrates, Acta Mater. 128 (2017) 418–427. https://doi.org/10.1016/J.ACTAMAT.2017.02.021.

[56] R. Drehmann, T. Grund, T. Lampke, B. Wielage, C. Wüstefeld, M. Motylenko, D. Rafaja, Essential Factors Influencing the Bonding Strength of Cold-Sprayed Aluminum Coatings on Ceramic Substrates, J. Therm. Spray Technol. 27 (2018) 446–455. https://doi.org/10.1007/S11666-018-0688-0/FIGURES/13.

[57] X.T. Luo, G.J. Yang, C.J. Li, K. Kondoh, High strain rate induced localized amorphization in cubic BN/NiCrAl nanocomposite through high velocity impact, Scr. Mater. 65 (2011) 581–584. https://doi.org/10.1016/J.SCRIPTAMAT.2011.06.030.

[58] D.M. Chun, S.H. Ahn, Deposition mechanism of dry sprayed ceramic particles at room temperature using a nano-particle deposition system, Acta Mater. 59 (2011) 2693–2703. https://doi.org/10.1016/J.ACTAMAT.2011.01.007.

[59] A.M. Vilardell, N. Cinca, I.G. Cano, A. Concustell, S. Dosta, J.M. Guilemany, S. Estradé, A. Ruiz-Caridad, F. Peiró, Dense nanostructured calcium phosphate coating on titanium by cold spray, J. Eur. Ceram. Soc. 37 (2017) 1747–1755. https://doi.org/10.1016/J.JEURCERAMSOC.2016.11.040.

[60] K.H. Ko, J.O. Choi, H. Lee, Intermixing and interfacial morphology of cold-

sprayed Al coatings on steel, Mater. Lett. 136 (2014) 45–47. https://doi.org/10.1016/J.MATLET.2014.07.142.

[61] K. Balani, A. Agarwal, S. Seal, J. Karthikeyan, Transmission electron microscopy of cold sprayed 1100 aluminum coating, Scr. Mater. 53 (2005) 845–850. https://doi.org/10.1016/J.SCRIPTAMAT.2005.06.008.